Research Article

Nano Research
2022, 15(5): 4334–4343

ISSN 1998-0124 CN 11-5974/O4
https://doi.org/10.1007/s12274-022-4069-0

Phytic acid-modified CeO_2 as Ca^{2+} inhibitor for a security reversal of tumor drug resistance

Zhimin Tian[1,§], Junlong Zhao[2,§], Shoujie Zhao[3,§], Huicheng Li[4], Zhixiong Guo[1], Zechen Liang[1], Jiayuan Li[1], Yongquan Qu[1] (✉), Dongfeng Chen[5] (✉), and Lei Liu[5] (✉)

[1] *Department Key Laboratory of Special Functional and Smart Polymer Materials of Ministry of Industry and Information Technology, School of Chemistry and Chemical Engineering, Northwestern Polytechnical University, Xi'an 710072, China*
[2] *State Key Laboratory of Cancer Biology, Department of Medical Genetics and Developmental Biology, Fourth Military Medical University, Xi'an 710032, China*
[3] *Department of General Surgery, Tangdu Hospital, Fourth Military Medical University, Xi'an 710038, China*
[4] *The State Key Laboratory of Cancer Biology, Department of Biochemistry and Molecular Biology, School of Basic Medicine, Fourth Military Medical University, Xi'an 710032, China*
[5] *Department of Gastroenterology, Daping Hospital, Army Medical University, Chongqing 400042, China*
[§] *Zhimin Tian, Junlong Zhao, and Shoujie Zhao contributed equally to this work.*

Received: 26 October 2021 / **Revised:** 3 December 2021 / **Accepted:** 13 December 2021

ABSTRACT

Ca^{2+} plays critical roles in the development of diseases, whereas existing various Ca regulation methods have been greatly restricted in their clinical applications due to their high toxicity and inefficiency. To solve this issue, with the help of Ca overexpressed tumor drug resistance model, the phytic acid (PA)-modified CeO_2 nano-inhibitors have been rationally designed as an unprecedentedly safe and efficient Ca^{2+} inhibitor to successfully reverse tumor drug resistance through Ca^{2+} negative regulation strategy. Using doxorubicin (Dox) as a model chemotherapeutic drug, the Ca^{2+} nano-inhibitors efficiently deprived intracellular excessive free Ca^{2+}, suppressed P-glycoprotein (P-gp) expression and significantly enhanced intracellular drug accumulation in Dox-resistant tumor cells. This Ca^{2+} negative regulation strategy improved the intratumoral Dox concentration by a factor of 12.4 and nearly eradicated tumors without obvious adverse effects. Besides, nanocerias as pH-regulated nanozyme greatly alleviated the adverse effects of chemotherapeutic drug on normal cells/organs and substantially improved survivals of mice. We anticipate that this safe and effective Ca^{2+} negative regulation strategy has potentials to conquer the pitfalls of traditional Ca inhibitors, improve therapeutic efficacy of common chemotherapeutic drugs and serves as a facile and effective treatment platform of other Ca^{2+} associated diseases.

KEYWORDS

Ca^{2+} nano-inhibitor, nanoceria, tumor drug resistance, phytic acid, nanozyme

1 Introduction

As a ubiquitous intracellular second messenger, Ca^{2+} has been well-established to play critical biological roles in the metabolic homoeostasis, signaling pathway, and development [1, 2]. Hence, numerous diseases (e.g., neurodegenerative disorders, cardiovascular disease, hypertension, diabetes, and tumors) are generally accompanied with the abnormal expression of Ca^{2+} signaling [3–6]. Besides, a variety of viruses including SARS-CoV-2 can modulate intracellular Ca^{2+} expression to facilitate virus infection and replication inside host cells [7]. In particular, the intracellular Ca^{2+} levels are crucial in mediating tumorigenesis as well as tumor progression [4, 6, 8]. Thereafter, various Ca regulation methods such as Ca^{2+} antagonist, hormones, and Ca-supplemental agents have been developed with the expectation to realize the successful disease treatments. However, the clinical applications of those Ca regulation methods have been greatly restricted due to their high toxicity, poor reversal efficacy, and nonspecific action [9–12]. Therefore, it is urgent to develop safe, efficient, and facile Ca^{2+} regulation strategy to satisfy practical demands.

With the rapid development of nanoscience and nanotechnology in modern medicine, nanomaterials have shown their great potentials to improve human living standards as well as disease therapy [13–23]. Specifically, nanomaterials have been designed to greatly overload the intracellular Ca^{2+} levels for tumor therapy [22–24]. However, since the abnormally high levels of Ca^{2+} might induce severe side effects including renal injury and cardiac arrest, the intracellular Ca concentration must be dedicatedly balanced within a narrow window to maintain normal Ca homeostasis [25, 26]. Thus, an attractive Ca regulatory strategy should mitigate Ca^{2+}-related cytotoxicity to guarantee the high safety of treatments. Considering the powerful and dual roles of Ca^{2+} in living organisms, to design a negative regulation strategy of Ca regulation by decreasing the intracellular Ca^{2+} level in a controllable manner is of great value in the treatments of various Ca-related diseases as well as tumors.

Address correspondence to Yongquan Qu, yongquan@nwpu.edu.cn; Dongfeng Chen, chendf@tmmu.edu.cn; Lei Liu, liulei84207@tmmu.edu.cn

It has been well documented that excessive Ca^{2+} can promote the intracellular Ca^{2+}-involved proliferation and provide a survival pathway for cancer cells after drug treatments, thereby decreasing the efficacy of chemotherapeutic drugs. Thus, higher cellular Ca^{2+} level is recognized as an essential characteristic of drug-resistant tumor cells, which is a major obstacle for the long-term efficacy of chemotherapeutic drugs [4, 8, 27–29]. Generally, high doses and/or various combinations of chemotherapeutic drugs are used to achieve effective therapy. However, such a temporary relief, regardless of the negative consequences of chemotherapeutic drugs, is inadvisable. Despite the intensive efforts to overcome drug resistance, only limited achievements have been realized. Herein, we design an unprecedentedly safe and efficient nanoscale platform to effectively remove the excessively expressed intracellular Ca^{2+} for reversal of tumor drug resistance and demonstrate the high feasibility of the intracellular Ca^{2+} negative regulation strategy for disease treatments. Both *in vitro* cellular and *in vivo* animal evaluations highlight that this strategy provides a facile, safe, and efficient platform for the reversal of tumor drug resistance, showing its great potentials for clinical applications.

2 Results and discussion

2.1 Design of intracellular Ca^{2+} negative regulation

Extensive examination of literatures emphasizes that high level of the intracellular free Ca^{2+} is believed to activate drug-transporting proteins (such as P-glycoprotein, P-gp) to efflux chemotherapeutic drugs out of tumor cells, ultimately reducing the efficacy of chemotherapy and leading to multidrug resistance. Previous studies have suggested that a rise in cytoplasmic Ca^{2+} level stimulates P-gp overexpression in tumor cells [27–29]. Thus, suppression of P-gp expression by regulating intracellular Ca^{2+} level offers an opportunity to overcome tumor drug resistance. The blockage of Ca^{2+} channels with Ca^{2+} antagonists has been demonstrated to exert beneficial effects in cancer cells by downregulating P-gp expression. However, the toxicity of those Ca blockers limits their potential clinical use [9, 10].

Inspired by the above cognitions, here, the phytic acid (PA)-modified porous nanorods of CeO_2 (CePA) have been rationally designed and experimentally demonstrated as an unprecedentedly safe and efficient platform to effectively enable the intracellular Ca^{2+} negative regulation through cleating between PA and Ca^{2+}, and successfully reverse tumor drug resistance (Scheme 1). Doxorubicin (Dox), which is severely limited in clinical therapy due to serious drug resistance, was selected as a model chemotherapeutic drug [30–32]. PA, an Food and Drug Administration (FDA)-approved natural product in many plant tissues (e.g., rice bran and seeds) as a tonic, food additive, antioxidant, preservative, and stabilizer, was chosen as a safe Ca nano-inhibitor for down-regulating the intracellular Ca^{2+} level due to the outstanding coordination ability between Ca^{2+} and PA [33–35].

Moreover, Dox as a commonly used chemotherapy drug can induce serious cardiotoxicity and hepatotoxicity due to the reactive oxygen species (ROS)-mediated oxidative damage and subsequent apoptosis of normal cells [30–32]. Therefore, reducing the side effects of Dox on normal cells is also highly expected. Due to high antioxidant capability of CeO_2 nanozyme for the degradation of ROS [36–43], the porous nanoceria (CeO_2) was used as an adjuvant medicine to alleviate Dox-induced oxidative stress in normal cells [32]. Therefore, the CePA nanozymes are expected to serve as a highly efficient Ca^{2+} nano-inhibitor, reducing Ca^{2+} levels in drug-resistant tumor cells, inhibiting P-gp overexpression, and increasing intracellular accumulation of drugs.

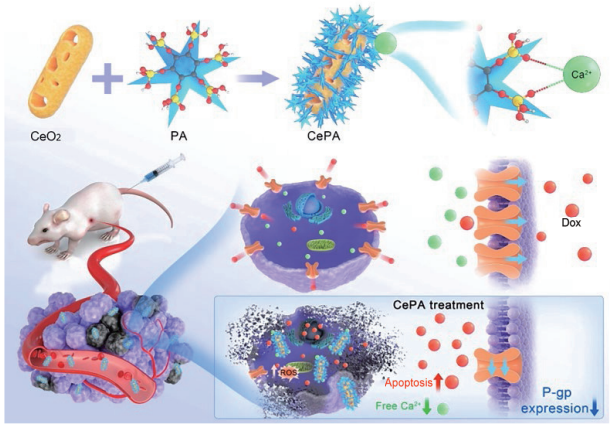

Scheme 1 Synthetic procedures of CePA and mechanism for drug resistance reversal via Ca^{2+} negative regulation. PA-modified porous nanorods of CeO_2 were demonstrated as an efficient nano-inhibitor to overcome drug resistance through coordination between PA and Ca^{2+}. After the nano-inhibitor enters the body, it reaches the tumor tissue mainly through the blood vessels, effectively scavenging Ca^{2+}, significantly suppresses P-gp expression and significantly enhances the intracellular Dox accumulation in drug-resistant tumor cells, thus achieving highly effective chemotherapy.

2.2 Synthesis and characterizations of CePA

Hydrothermally synthesized CeO_2 showed a porous rod-like morphology with fluorite phase, as revealed from transmission electron microscopy (TEM) and X-ray diffraction (XRD) pattern (Fig. S1 in the Electronic Supplementary Material (ESM)) [44]. Afterwards, CePA hybrids were synthesized by immersing CeO_2 into aqueous PA solution (2 wt.%) for 12 h and subsequent centrifugal separation. TEM and XRD characterizations indicated the preserved morphological features and phases of CeO_2 during treatment (Fig. 1(a) and Fig. S1(b) in the ESM). To probe the surface states of CePA, Fourier transform infrared (FT-IR) spectroscopy and TEM elemental mapping were performed. Compared with CeO_2, the FT-IR spectrum of CePA showed two new emerging absorption peaks at 1,230 and 1,651 cm^{-1} due to the P=O stretching mode of PO_4^{3-} and the increased peak at 3,510 cm^{-1} due to the hydroxyl of PA, confirming the successful modification of CeO_2 by PA (Fig. 1(b)). In comparision with a near neutral potential (2.6 mV) of CeO_2 with the abundant interfacial hydroxyl, the zeta potential of CePA decreased to −41.2 mV, also supporting the successful conjugation of the negatively charged PA on CeO_2 (Fig. 1(c)). TEM elemental mapping images further proved the formation CePA hybrids due to the homogeneous distribution of Ce, O, and P elements in CePA (Fig. 1(d)). The loadings of PA in the CePA was ~ 4.7 wt.% determined by the inductively coupled plasma mass spectrometry (ICP-MS) through the quantification of the P element.

2.3 Coordination ability of Ca^{2+}

Afterwards, the Ca^{2+} coordination capability of CeO_2 and CePA was evaluated in tris-HCl buffer solution (50 mM, pH 7.4, and 50 μM Ca^{2+}) by a Ca^{2+} probe, o-cresolphthalein complexone. CeO_2 showed the negligible Ca^{2+} coordination capability. Impressively, CePA showed significant Ca^{2+} coordination activity (> 70%, Fig. 1(e)), enabling CePA as a potential Ca^{2+} nano-inhibitor for *in vitro* and *in vivo* investigations. The Ca^{2+} spectral absorption further revealed the outstanding Ca^{2+} coordination capability of CePA in a dose-dependent performance, as evidenced by a decrease of spectral absorption at 570 nm (Fig. 1(f)) [45]. The corresponding solution colors from dark violet to light purple with the increased doses of CePA indicate the promises as cytoplasmic Ca^{2+} nano-inhibitor for reversing tumor drug resistance (Fig. 1(g)).

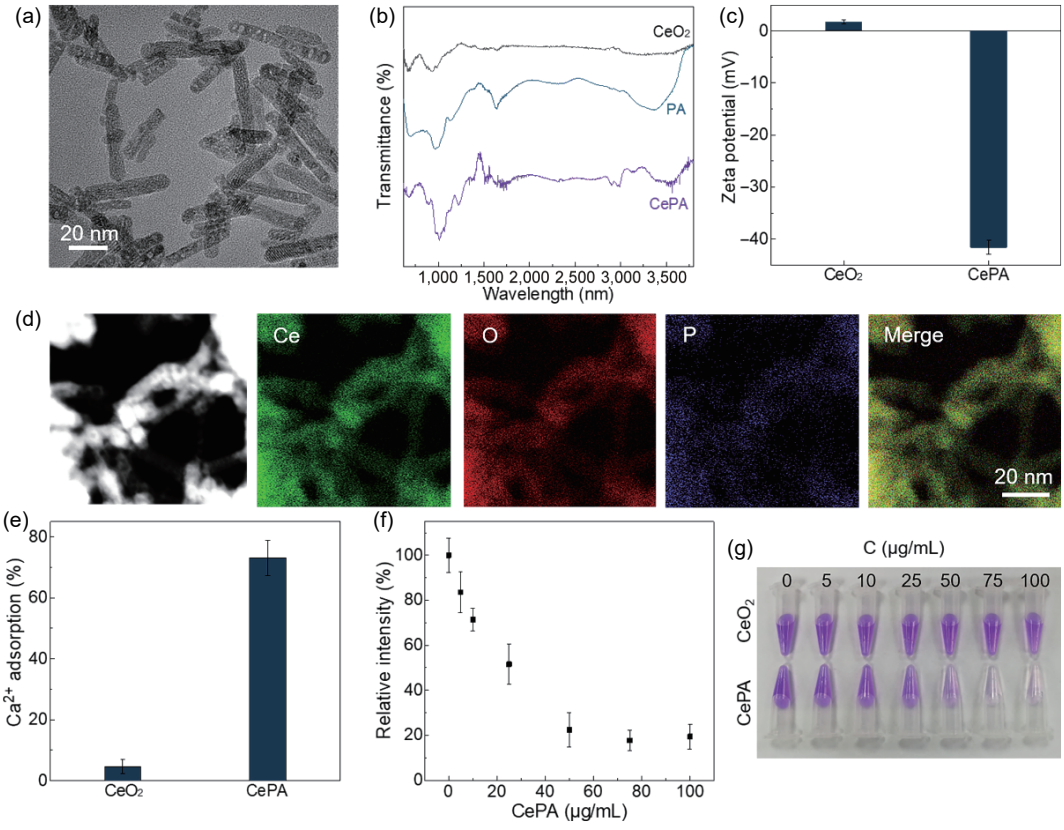

Figure 1 Characterizations and Ca^{2+} coordination ability of CePA. (a) TEM image of CePA; (b) FT-IR spectra of PA, CeO_2, and CePA; (c) zeta potentials of CeO_2 and CePA; (d) EDS element mapping images of CePA; (e) the Ca^{2+} levels in the presence of CeO_2 and CePA; (f) the relative intensity of Ca^{2+} (1 μg/mL) after being treated with different concentrations of CePA; (g) representative images of Ca^{2+} solutions treated by CeO_2 and CePA in various dosage.

2.4 pH-dependent ROS scavenging activity and cytotoxicity evaluation

Due to the severe Dox-induced oxidative stress and the high antioxidant ability of nanoceria as nanozyme to scavenge drug-induced ROS [32, 42], herein, we anticipated that nanocerias would suppress or even prevent adverse effects of Dox on normal organs. Then, the ROS scavenging activity of CeO_2 and CePA was evaluated by calibration from the standard catalase and superoxide dismutase (SOD) assay kits. CePA showed better H_2O_2 elimination than CeO_2 at the same dose, indicating its higher catalase-like performance (Fig. S2(a) in the ESM). For SOD-mimic activity, both CeO_2 and CePA exhibited enhanced performance with the increase of catalyst concentration (Fig. S2(b) in the ESM). Consistent with the catalase-like results, the SOD-like activity of CePA was higher than that of CeO_2 at each concentration, demonstrating the higher antioxidant activity of CePA over CeO_2. The ratio of Ce^{3+}/Ce^{4+} plays a pivotal role in their cpability of ROS scavenging [32, 39–42]. Herein, X-ray photoelectron spectra (XPS) of CeO_2 and CePA suggested their similar surface Ce^{3+} fractions (Fig. S3 in the ESM), indicating that the surface defect concentration was not the primary factor for the difference in their antioxidative capabilities. Considering PA as a natural antioxidant [33, 34], the conjugation of PA on CeO_2 might contribute to the increased antioxidant performance of CePA. Meanwhile, the cytotoxicity experiments showed that both CeO_2 and CePA delivered a better protective capability than free PA (Fig. S4 in the ESM). Importantly, the ROS scavenging efficiency of both CeO_2 and CePA was pH dependent, and their total free radical scavenging activity was significantly higher in normal physiological environments than in weakly acidic conditions (Fig. S5 in the ESM). The aberrant glycolytic metabolism of the tumor microenvironment (TME) causes pH of tumor tissues to be less than the normal physiological value. Hence, nanocerias showed their high potential to selectively alleviate the adverse drug effects on normal organs during chemotherapy.

Before evaluating their capability for the reversal of drug resistance, the biosafety of CeO_2 and CePA was studied using normal human liver cells (LX-2) and Dox-resistant human hepatic carcinoma cells (HepG2/ADR). No obvious cytotoxicity was observed in either cell lines, suggesting their high biocompatibility (Fig. S6 in the ESM). Then, the cellular uptake of CeO_2 and CePA in HepG2/ADR cells was found to be dose and time dependent by ICP-MS (Fig. S7 in the ESM). As shown in TEM images (Fig. S8 in the ESM), CeO_2 and CePA were both observed in the cytoplasm after tumor cells uptake, indicating the successful uptake by the cells and offering a solid preliminary basis for their biological applications.

2.5 Reversing the Dox resistance *in vitro*

Next, we evaluated the influence of the CeO_2 and CePA on Dox sensitivity in the Dox-resistant tumor cells (HepG2/ADR). As expected, Dox showed limited toxicity in HepG2/ADR cells, even at a high concentration of 30 μM (Fig. S9(a) in the ESM). Notably, CePA significantly enhanced the antitumor activity of the Dox in the HepG2/ADR cells, demonstrating its high capability to overcome the Dox-induced drug resistance (Fig. 2(a)). When the CePA dose was > 50 μg/mL, the antagonizing Dox-resistance activity of CePA reached saturation (Fig. S9(b) in the ESM). Hence, 50 μg/mL CePA was used to investigate the reversal of Dox resistance, except where otherwise indicated. While, CeO_2 barely enhanced the therapeutic efficacy of Dox in HepG2/ADR cells under same conditions, suggesting that the surface conjugation of PA on CeO_2 played critical roles in the enhanced antitumoral efficacy of Dox in drug-resistant HepG2/ADR cells.

Thereafter, the flow cytometry and fluorescence images further demonstrated that the intracellular Dox concentration was

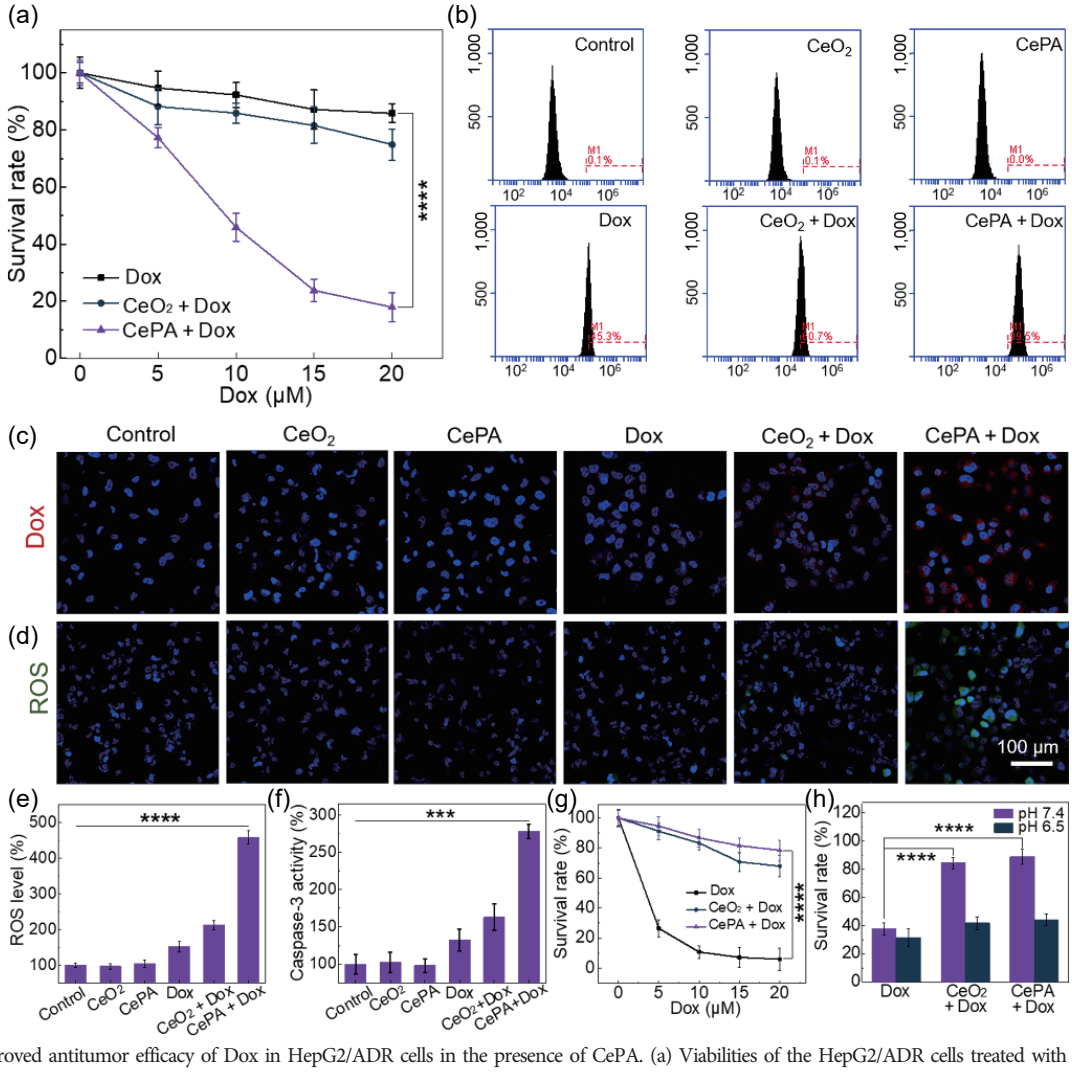

Figure 2 Improved antitumor efficacy of Dox in HepG2/ADR cells in the presence of CePA. (a) Viabilities of the HepG2/ADR cells treated with CeO_2 or CePA (CeO_2: 50 μg/mL, CePA: 50 μg/mL) for 6 h, and co-incubated with Dox (5–20 μM) for another 6 h. (b) Corresponding red fluorescence intensity of Dox in HepG2/ADR cells under various treatments was measured by flow cytometry. (c) Confocal microscopy images of HepG2/ADR cells treated with DPBS (control), Dox, CeO_2, CePA, CeO_2 + Dox, and CePA + Dox. All the groups were treated with Dox at the same concentration (10 μM). Dox: red fluorescence; cell nucleus: blue fluorescence. (d) ROS fluorescence images were captured in HepG2/ADR cells treated with DPBS, Dox, CeO_2, CePA, CeO_2 + Dox, and CePA + Dox.. ROS: green fluorescence; cell nucleus: blue fluorescence. (e) Quantitative analysis of ROS levels for HepG2/ADR cells under various treatments using 2',7'-dichlorofluorescein diacetate as a probe (n = 3). (f) Relative caspases-3 levels induced by Dox in the presence or absence of the CeO_2 or CePA (n = 3). (g) Viabilities of the LX-2 cells treated with CeO_2 or CePA (CeO_2: 50 μg/mL, CePA: 50 μg/mL) for 6 h, and co-incubated with Dox (5–20 μM) for another 6 h (n = 3). (h) Relative cell viabilities of LX-2 pretreated with CeO_2 or CePA (CeO_2: 50 μg/mL, CePA: 50 μg/mL) under Dox (10 μM) treatments under neutral (pH 7.4) and acidic (pH 6.5) environments (n = 3). Data are presented as means ± SD, ***P < 0.001 and ****P < 0.0001 (unpaired Student's two-sided t-test analysis).

significantly enhanced in HepG2/ADR cells protreated by CePA. Thus, CePA decreased efflux of Dox from HepG2/ADR cells (Figs. 2(b) and 2(c)) and thereby upregulated the intracellular ROS expression (Figs. 2(d) and 2(e)), leading to the greatly enhanced intracellular Dox accumulation by CePA, significantly raised cytotoxicity in HepG2/ADR cells and consequently increased caspase-3 activity (Fig. 2(f) and Fig. S10 in the ESM). Flow cytometry and TdT mediated dUTP nick-end labeling (TUNEL) also showed that after CePA pretreatment, Dox delivered a remarkable increase in the percentage of apoptotic HepG/ADR cells (Figs. S11 and S12 in the ESM), consistent with the results of caspase-3 expression (Fig. 2(f) and Fig. S10 in the ESM).

2.6 pH-dependent cytoprotective effect of nanocerias *in vitro*

Considering the side effects of Dox, we further analyzed the capability of nanocerias against the chemotherapy-induced cell injury on normal LX-2 cells. CeO_2 and CePA significantly improved viability of LX-2 cells treated by Dox (Fig. 2(g)). Importantly, the cytoprotective effects of nanocerias were strongly depended on the environmental pH, delivering the outstanding protection at pH 7.4 but poor cytoprotections at pH 6.5 (Fig. 2(h)). Further analysis of ROS and apoptosis also confirmed the above results (Figs. S13 and S14 in the ESM). Overall, CePA with high antioxidant activity is expected to suppress the side effects during tumor chemotherapy in normal cells and enhance chemotherapeutic activity in drug-resistant tumors.

2.7 Intracellular Ca^{2+} deprivation for reversing the drug resistance

Then, the mechanism of CePA against the drug resistance was explored. As previously reported [27–29], the increased intracellular level of free Ca^{2+} is closely related to tumor drug resistance. Based on the capability of CePA as Ca^{2+} nano-inhibitor resulting in intracellular Ca deficiency (Figs. 1(e)–1(g)) and the reversal of tumor Dox resistance (Figs. 2(a)–2(f) and Figs. S9–S11 in the ESM), we evaluated the capability of CePA for the deprivation of free intracellular Ca^{2+} in the Dox-resistant HepG2/ADR cells. CeO_2 showed a barely interferred intracellular Ca^{2+} level (Figs. 3(a) and 3(b)). Impressively, CePA treatment in

the HepG2/ADR cells for 6 h dramatically lowered the intracellular free Ca^{2+} level by 45% (Figs. 3(a) and 3(b)), indicating the capability of CePA as Ca^{2+} nano-inhibitor for regulating the intracellular Ca^{2+} level. Both western blotting and immunofluorescence staining analysis confirmed that CePA efficiently captured the intracellular Ca^{2+} and then markedly decreased the P-gp expression (Figs. 3(c) and 3(e)).

To further confirm CePA as a Ca^{2+} nano-inhibitor against the tumor drug resistance, CALP2, an agonist of Ca^{2+}, was used to prevent the activity of CePA. The experimental results showed that the CALP2 pretreatment significantly attenuated the capability of CePA against tumor drug resistance, further demonstrating the CePA-enabled reversal of tumor drug resistance through the Ca^{2+} negative regulation strategy (Fig. S15 in the ESM). Based on above analysis and mechanism investigations, CePA as Ca^{2+} nano-inhibitor efficiently captured the intracellular Ca^{2+} in the HepG2/ADR cells, significantly decreased the P-gp expression and greatly increased drug accumulation within the resistant tumor cells, ultimately reversing the drug resistance.

2.8 Biodistribution and biosecurity of nanocerias *in vivo*

Encouraged by the *in vitro* results, the HepG2/ADR tumor-bearing model in BALB/c nude mice was established to evaluate the potentials of CePA for reversal of Dox resistance *in vivo*. The biocompatibility of CeO_2 and CePA as the primary consideration was initially assessed. Primarily, main blood markers and histological analyses of the main organs showed no obvious abnormalities between the CeO_2/CePA-injected group and control group (Figs. S16 and S17 in the ESM). Meanwhile, after intravenous injection of CeO_2 and CePA, the biodistribution of naocerias in major organs decreased gradually overtime (Fig. S18(a) in the ESM), further suggesting that the nanocerias could be effectively removed out of the body. We then proved that the nanoceria could be excreted via urine (Fig. S18(b) in the ESM) [46]. All results demonstrated the high *in vivo* biocompatibility of CeO_2 and CePA. Conversely, 94% and 76% of Ce was retained in tumors after CeO_2 and CePA injection for 7 days, demonstrating tumor accumulation of CeO_2 and CePA. Such intratumor permeability and retention of two candidates facilitated their effective delivery into tumors for overcoming tumor drug resistance.

2.9 Improved chemotherapy by CePA *in vivo*

We then evaluated the overall therapeutic performance of CeO_2 and CePA against Dox-resistant tumors in HepG2/ADR tumor-bearing BALB/c nude mice. The tumor-bearing mice were randomly divided into six groups: control, Dox, CeO_2, CePA, CeO_2 + Dox, and CePA + Dox. The tumor volumes in the control and Dox groups were increased by factors of 12.1 and 10.8 on the 14th day, respectively (Fig. 4(a)), indicating the strong Dox-resistance developed in the tumor cells. Conversely, the combination of CePA and Dox completely restricted tumor growth (Fig. 4(a)), indicating the excellent efficacy of CePA for reversing chemotherapy resistance. CeO_2 and CePA groups also showed certain inhibitory activity against tumor growth, which could be attributed to the peroxidase-like activity of CeO_2 and CePA to convert the intratumoral H_2O_2 into toxic ·OH in TME [47, 48]. The digital images and average weight of tumors confirmed the tumor growth profiles (Figs. 4(b) and 4(c)). Significant weight loss (29.7%) of the tumor-bearing mice treated by Dox was observed due to the main adverse effect of chemotherapy (Fig. 4(d)). Notably, CeO_2 and CePA induced no significant weight change throughout the treatments, further verifying their biosafety and their potential protective effects against Dox-induced adverse effects *in vivo*.

The mechanism of CePA for restoring Dox-sensitivity was further revealed by histological analysis [49, 50]. Hematoxylin and eosin (HE) staining showed that compact tumor tissues were found for the Dulbecco's Phosphate Buffered Saline (DPBS, control)- and Dox-treated tumor-bearing mice (Fig. 4(e)). In contrast, large areas of apoptosis and necrosis in tumor tissues and more vacancies were observed after the combined CePA + Dox treatment, further suggesting that CePA was able to reverse tumor drug resistance, consistent with the tumor inhibition results (Figs. 4(a)–4(c)).

Similar results were observed in ROS, TUNEL, and caspase-3 staining images (Fig. 4(f) and Fig. S19 in the ESM). CePA + Dox combination treatment significantly strengthened the intratumoral ROS production by Dox (Fig. 4(f)), consistent with the CePA-induced increase of Dox level in tumor issues (Fig. 4(g)). Significant green fluorescence was observed in mice treated with CePA + Dox, suggesting the widespread DNA strand fragmentation and tumor cell apoptosis (Fig. S19(a) in the ESM). The apoptosis areas in the CePA + Dox group were significantly larger than those in other groups. Overlapping of the blue (nucleus) and green fluorescence again confirmed DNA fragmentation. Besides, the immunofluorescent staining demonstrated that the tumor tissues from the CePA + Dox-

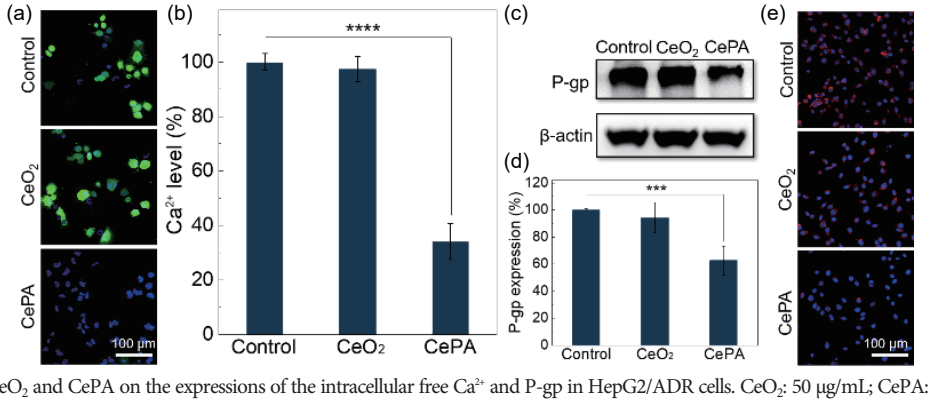

Figure 3 Influence of CeO_2 and CePA on the expressions of the intracellular free Ca^{2+} and P-gp in HepG2/ADR cells. CeO_2: 50 μg/mL; CePA: 50 μg/mL. (a) Confocal microscopy fluorescence imaging of the free Ca^{2+} changes via Fluo-3/AM green signal in HepG2/ADR cells incubated with CeO_2 and CePA for 12 h. (b) Quantitative analysis of the intracellular Ca^{2+} levels in HepG2/ADR cells treated with CeO_2 and CePA for 12 h. Cells exposed to CeO_2 or CePA were incubated with Fluo-3/AM, and then the intracellular free Ca^{2+} was monitored. Data are representative of three independent experiments. (c) The expression levels of P-gp on HepG2/ADR cells after 12 h incubation with CeO_2 and CePA detected by the western blot analysis. (d) Corresponding gray analysis of P-gp via western blot. Quantification of the expression of P-gp normalized to that of β-actin. Data were shown as the mean ± SD (n = 3). (e) Confocal microscopy of P-gp expression of HepG2/ADR cells treated with CeO_2 and CePA. P-gp: red fluorescence; cell nucleus: blue fluorescence. Data are presented as means ± SD, ***P < 0.001 and ***P < 0.0001 (unpaired student's two-sided t test analysis).

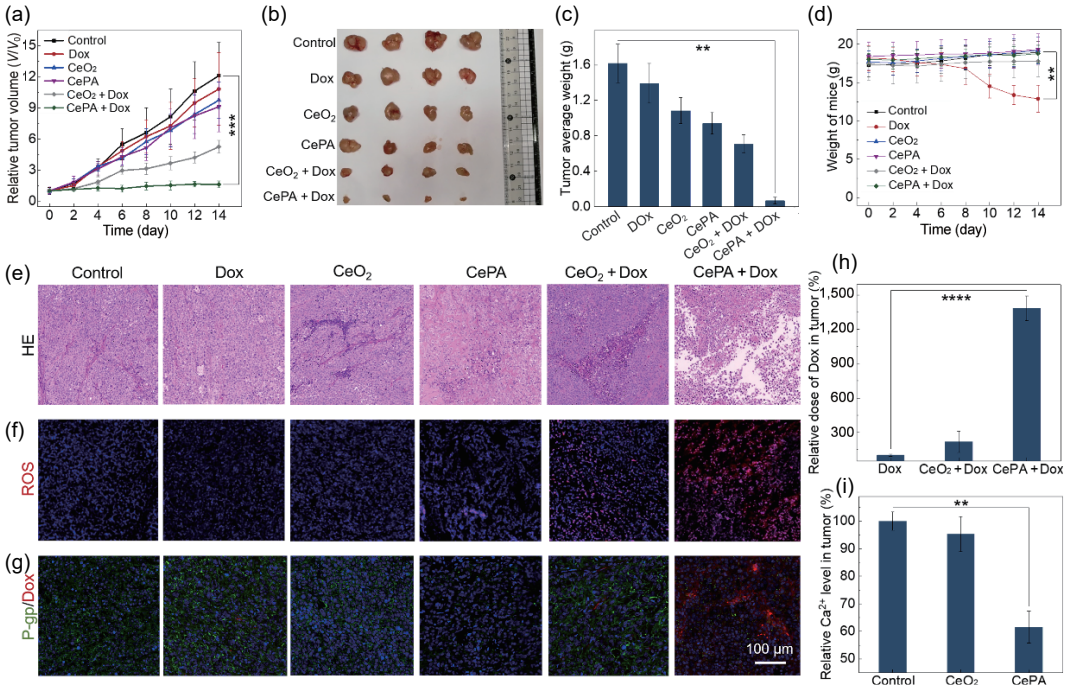

Figure 4 *In vivo* drug resistance reversal efficacy of CeO_2 and CePA. (a) Relative tumor volume in the mice receiving the indicated treatments (control, Dox, CeO_2, CePA, CeO_2 + Dox, and CePA + Dox; 5.0 mg/kg of Dox; 7 days apart for 2 consecutive injections beginning on day 1) over 14 days (n = 4). (b) Images of the tumors isolated from the tumor-bearing mice receiving indicated treatments. (c) Weights of the harvested tumor tissues. (d) The body weights of the tumor-bearing mice during treatments (n = 4). (e) HE staining of tumor tissues. (f) ROS staining for pathological changes of tumor tissues after various treatments. (g) Immunofluorescence analysis of the expression of P-gp in tumor region after various treatments. The nuclei were stained with DAPI (blue), P-gp (green), and Dox (red). (h) Fluorescent intensities of Dox in the tumor tissues after various treatments (n = 3). (i) Relative level of Ca^{2+} in the tumor tissues after various treatments (n = 3). Data are presented as means ± SD, $^{**}P < 0.01$ and $^{****}P < 0.0001$ (unpaired Student's two-sided t-test analysis).

treated mice showed the highest expression of caspase-3 (Fig. S19(b) in the ESM). Quantitatively, the tumor tissues treated by CePA + Dox showed the highest expression of caspase-3 (Fig. S20 in the ESM), implying that CePA enhanced the effect of Dox, consistent with the tumor inhibition data (Fig. 4).

P-gp expression of various groups was also monitored by immunofluorescent staining (Fig. 4(g)). CeO_2 exhibited no significant influence on the P-gp expression. Thus, the intratumoral Dox (red fluorescence) levels in the Dox-treated and CeO_2 + Dox treated groups were negligible. Comparatively, the expression of the intratumoral P-gp (green fluorescence) was markedly downregulated upon exposure to CePA, leading to the significantly enhanced the intratumoral Dox level of the CePA + Dox group. Then, the concentrations of Dox in tumor tissues after the CeO_2 and CePA treatments for 24 h were further identified by high-performance liquid chromatography. CePA markedly enhanced the tumor accumulation of Dox, which was 12.4-fold higher than that of the Dox-treated tumor tissues (Fig. 4(h)). Therefore, CePA reversed Dox resistance of tumor cells by downregulating P-gp expression, decreasing the efflux pump for Dox and enhancing intratumoral Dox retention. To verify the contribution of Ca^{2+} to tumor drug resistance, variation in intratumoral free Ca^{2+} concentration was measured for the control, CeO_2, and CePA groups. The intratumoral free Ca^{2+} level in the CePA group showed a significant decrease of 61.5% after 24 h treatment (Fig. 4(i)), consistent with the decrease of P-gp expression (Fig. 4(h)). Thus, the results again demonstrated that CePA as Ca^{2+} nano-inhibitor overcame tumor Dox resistance and restored sensitivity by inducing Ca deficiency in tumor cells, triggering P-gp downregulation and increasing intratumoral Dox retention.

2.10 Nanocerias protect against Dox-induced heart and liver injury

Meanwhile, Dox can induce serious toxic adverse effects in major organs due to ROS-mediated DNA damage and apoptosis of normal cells, especially cardio- and hepatotoxicity [30–32, 51]. Besides the capability of CePA for reversing drug resistance, the protective benefits of CeO_2 and CePA against Dox-induced cardiac injury and liver damage in mice were evaluated. The body weight of the Dox-treated mice significantly decreased (~ 32%) (Fig. 4(d)), compared with the DPBS-treated mice, indicating that Dox caused severe systemic injury. More importantly, 60% of mice treated by Dox alone died within 28 days, whereas all mice pretreated with CeO_2 and CePA survived up after Dox treatment during same period (Fig. 5(a)). Besides, the plasma levels of lactate dehydrogenase (LDH, specific marker of cardiac injury), creatine kinase isoenzyme myocardial band (CK-MB, specific marker of cardiac injury), alanine aminotransferase (ALT, specific marker of liver injury), and aspartate aminotransferase (AST, specific marker of liver injury) of the Dox group were markedly higher than those in the control group (Figs. 5(b)–5(d)). Conversely, the levels of these serum markers in the CeO_2 + Dox and CePA + Dox groups showed bare changes compared with the control group (Figs. 5(b)–5(d)), further indicating that CeO_2 and CePA significantly inhibited Dox-induced heart and liver injury.

HE-stained cardiac tissues indicated that the Dox group mice exhibited myofibrillar loss (Fig. 5(e)), vacuolization and swelling. Meanwhile, the hepatic tissues taken from the Dox group showed severe pathological alterations (blood vessel congestion and necrosis) (Fig. 5(f)). As expected, no obvious myocardial damages and liver injury were found in the CeO_2 + Dox and CePA + Dox groups. Similar to the cytoprotective results (Fig. 2(g) and Figs. S13 and S14 in the ESM), CeO_2 and CePA also effectively degraded the Dox-induced oxidative stress in the heart and liver (Fig. S21 in the ESM). Similar results of TUNEL and caspase-3 staining of cardiac tissue and hepatic tissue sections confirmed that CeO_2 and CePA attenuated Dox-induced apoptosis in the heart and liver (Figs. S22 and S23 in the ESM). Overall, CePA is a

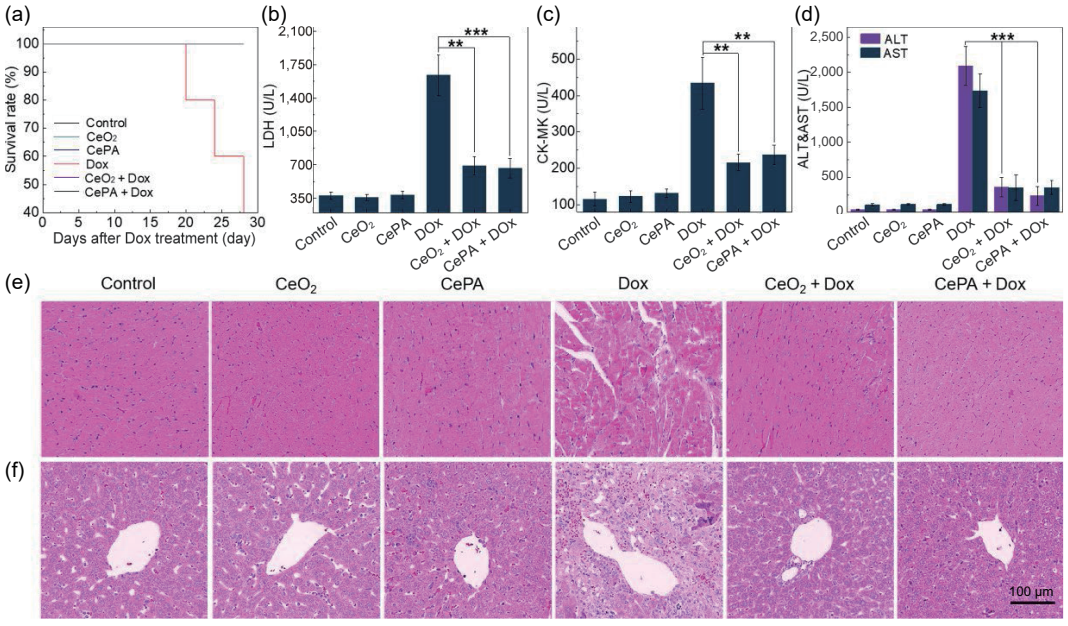

Figure 5 Detoxification of Dox-induced cardiotoxicity and hepatic injury by CeO_2 and CePA. (a) Survival rates of mice intravenously injected with Dox (5 mg/kg) or/and pre-treated with CeO_2 and CePA (n = 3). (b)–(d) Changes in serum levels of LDH, CK-MB, ALT, and AST after various treatments (n = 3). LDH and CK-MB: serum marker of cardiac injury; ALT and AST: serum markers of liver injury. (e) HE staining of sections from the cardiac tissues in mice after various treatments. (f) HE staining of sections from the hepatic tissues in mice pre-treated with CeO_2 and CePA against Dox. Scale bar: 100 μm. Data are presented as means ± SD, $^{**}P < 0.01$ and $^{***}P < 0.001$ (unpaired Student's two-sided t-test analysis).

safe Ca^{2+} nano-inhibitor for the reversal of tumor drug resistance and an efficient antioxidant against Dox-induced oxidative stress in normal organs, indicating its therapeutic potential.

3 Conclusions

In a summary, a facile and efficient negative regulation strategy of intracellular Ca^{2+} has been dedicatedly designed and successfully developed to overcome tumor drug resistance while preventing from Dox-induced organ damage. PA in the nano-inhibitor, as a Ca^{2+} coordination agent, efficiently deprives the intracellular excessive free Ca^{2+}, and significantly suppresses expression and activity of P-gp to avoid drug efflux. The high safety of the nano-inhibitor CePA is illustrated by no obvious systemic damage as well as relief of chemotherapy-induced oxidative stress in the major organs, due to its high antioxidant capability. The synergistic effect of the Dox and CePA treatment improves the efficacy of the commonly chemotherapeutic agent and decreases the side effects. This negative regulation strategy of intracellular Ca^{2+} with features of high safety and efficacy not only brings new insights on the tumor drug resistance, and also provides an alternative methodology for other Ca related diseases, such as Ca poisoning, atherosclerosis and neurodegenerative diseases, even COVID-19.

4 Experimental

4.1 Chemicals

Cerium(III) nitrate hexahydrate, Na hydroxide, PA (50%), Ca chloride, Triton X-100, and hydrogen peroxide (3%) were obtained from Sigma-Aldrich Co. (USA). Dulbecco's modified eagle medium, penicillin-streptomycin (100×), fetal bovine serum (FBS), DPBS, 4,6-diamidino-2-phenylindole (DAPI), dihydroethidium (DHE), alamarBlue, and 2',7'-dichlorofluorescein diacetate (DCFH-DA) were purchased from Thermo Fisher. The Dox was purchased from Meilunbio. The primary antibody (Anti-P-gp; ab170904; Abcam biotechnology) was used for western blot and immunofluorescence staining. Ultrapure water (18.2 MΩ/cm), purified by a Milli-Q system was used throughout the experiments.

4.2 Synthesis of CeO_2 and CePA

CeO_2 was synthesized through a two-step hydrothermal method according to our previous report [44]. For a typical preparation of PA-modified CeO_2, 50 mg of CeO_2 were dispersed in 100 mL of 2.0 wt.% aqueous solution of PA. The mixed solutions were ultrasonicated for 1 h and then vigorously stirred at ambient temperature for 12 h. The hybrids were collected by centrifugation at 12,000 rpm for 10 min, repeatedly washed with ultrapure water for three times and dried at 50 °C. Then, the CePA hybrids were dispersed in H_2O with a concentration of 5 mg/mL by ultrasonication for 20 min.

4.3 Characterizations

TEM and energy dispersive spectroscopy (EDS) mapping were examined on a JEM-2100F filed emission electron microscope with an acceleration voltage of 200 kV. XRD patterns of samples were determined using a Shimadzu X-ray diffractometer (Model 6000) with Cu Kα radiation at a scanning rate of 5°/min in the 2θ range from 10° to 90°. XPS spectra were performed on Thermo Electron Model K-Alpha. Surface charge analysis of samples were detected by Zetasizer Nano ZS 90 (Malvern Instruments). The organ and tissue distributions of cerium were measured by ICP-MS, Thermo. FT-IR spectroscopy were performed on Thermo FT-IR spectrophotometer (NICOLET 6700). Fluorescence imaging photos were taken through confocal laser scanning microscopy (Nikon A1). The SOD activity of nanoceria were determined by hydroxylamine assay-developed from xanthine oxidase assay (SOD assay kits, Beyotime, China). The levels of H_2O_2 were analyzed by a hydrogen peroxide assay kit (Beyotime, China).

4.4 Cell culture

LX-2, HepG2, and HepG2/ADR cells were cultured in Dulbecco's modified Eagle's medium (DMEM) supplemented with 10% FBS and 1% antibiotics (penicillin-streptomycin) in a humidified atmosphere at 37 °C (5% CO_2 and 95% air).

4.5 Cytotoxicity assay

LX-2 cells were seeded into 96-well plates, adjusted to a density of 2×10^3 per well and incubated in 5% CO_2 at 37 °C for 12 h. Subsequently, LX-2 cells were treated with CeO_2 and CePA at various concentrations (0.1–1,000 μg/mL) for 24 h. After removal of cellular DMEM medium, the LX-2 cells were treated with 100 μL of 10% alamarBlue at 37 °C for 2 h. Finally, the cell survival rates were determined by the standard alamarBlue assay. Each experiment was repeated at least for three times independently.

4.6 Intracellular ROS and cell apoptosis

The determination of ROS levels was via fluorescent imaging. Typically, the LX-2 and HepG2/ADR cells were planted in a confocal dish with a density of 10^5 cells/dish for 12 h for six different groups: (a) control (DPBS), (b) CeO_2, (c) CePA, (d) Dox, (e) CeO_2 + Dox, and (f) CePA + Dox. After the cells adhered, the CeO_2 and CePA were added and incubated with cells for 6 h, sequentially. The concentration of CeO_2 and CePA was controlled at 50 μg/mL. Finally, the Dox (20 μM) was added and coincubated for 1 h at 37 °C. Afterwards, the cells were stained with DCFH-DA (10 μM) and the levels of the intracellular hydroxyl radicals were monitored by confocal laser scanning microscopy (Nikon A1). Similarly, after incubation under various treatments, the LX-2 and HepG2/ADR cells were stained by Annexin V-FITC/PI Apoptosis Detection Kit (Thermo Fisher). The levels of apoptosis were monitored by flow cytometry (BD Accuri C6).

4.7 Western blot analysis

HepG2/ADR cells were cultured in 6-well plates at a density of 6×10^5 cells/well. Then, the cells were treated with DMEM (control group), CeO_2, and CePA for 6 h, respectively. Subsequently, the HepG2/ADR cells were washed by cold fresh DPBS for three times, collected and then lysed (RIPA Lysis Buffer). The total proteins were distilled through the addition of the total protein extraction kit and the protein concentrations were tested by BCA protein assay kit (Beyotime, China). Afterwards, total proteins were loaded in the wells of 10% Na dodecyl sulfate-polyacrylamide gel electrophoresis and then transferred to polyvinylidene fluoride (PVdF) membranes. The membranes were incubated with P-gp antibodies (Abcam, dilution 1:1,000) and β-actin (Invitrogen, dilution 1:2,000) for 4 h. Then, the membranes were blocked by 5% non-fat milk (Bio-Rad) overnight at 4 °C, then washed for three times with Western washing buffer (TBS-T), and incubated with horseradish peroxidase-conjugated secondary antibody (Invitrogen, dilution 1:5,000) for 1 h at room temperature. After washing for three times with TBS-T buffer, the protein blots could be analyzed using the chemiluminescence system.

4.8 Viability of HepG2/ADR and LX-2 cells treated with Dox

To confirm HepG2/ADR cells were resistant to Dox, the HepG2/ADR cells (2×10^3 cells/well) were cultured in 100 μL of medium (96-well plates) at 37 °C for 12 h. Then, the fresh 100 μL of medium containing different concentrations of Dox (0–30 μM) was added. After the incubation for 6 h, the alamarBlue method was performed to evaluate cell viabilities. Furthermore, the viability of non-resistant liver tumor cells (HepG2) and LX-2 cells with Dox treatment at different concentrations was further evaluated by the same method.

4.9 Viabilities of HepG2/ADR and LX-2 cells after CeO_2/CePA preincubation with Dox treatments

HepG2/ADR and LX-2 cells (2×10^3 cells/well) were seeded into 96-well plates and cultured in DMEM medium at 37 °C for 12 h. Subsequently, the CeO_2 (50 μg/mL) and CePA (50 μg/mL) were added and incubated with cells for 6 h, respectively. Finally, Dox with various concentrations (0–30 μM) was added and co-incubated for 6 h at 37 °C. Relative cell viabilities were measured by the alamarBlue method.

4.10 Cellular uptake assay

HepG2/ADR cells were seeded in 6-well plates and cultured at 37 °C for 12 h. Subsequently, the HepG2/ADR cells were incubated with CeO_2 and CePA in various dosage (10–200 μg/mL) with various time (1–12 h) at 37 °C, then washed with cold DPBS for three times, and finally harvested in aqua regia until the complete digestion of the cells. Afterwards, the solutions were diluted with water to reach a final volume of 10 mL. The Ce element content was determined by ICP-MS for three times for each treatment.

4.11 Cellular uptake of CeO_2 and CePA by TEM

HepG2/ADR cells (3×10^5 cells/well) was seeded in 60 mm culture dishes. CeO_2 (50 μg/mL) and CePA (50 μg/mL) in the DMEM medium were added and incubated with the HepG2/ADR cells for 6 h. Then HepG2/ADR cells were collected and washed with cold DPBS for three times. Finally, paraformaldehyde solution (2.5% in DPBS buffer) was employed to fix HepG2/ADR cells at 4 °C for 12 h and then surface-embedded in epoxy resin. Transverse thin-sections were cut, transferred to a carbon-coated grid for TEM examination (Hitachi-7650, Hitachi) at 80 kV.

4.12 TUNEL assay

HepG2/ADR cells were seeded in the confocal dishes at a density of 10^5 cells/dish for 12 h. Subsequently, the CeO_2 (50 μg/mL) and CePA (50 μg/mL) were added and incubated with cells for 6 h. Dox (20 μM) was then added and co-incubated for another 6 h at 37 °C. Afterwards, the HepG2/ADR cells were fixed with 4% formaldehyde for 30 min at 4 °C, permeabilized with Triton X-100 (1%, DPBS) and washed with DPBS for three times. Finally, the HepG2/ADR cells were incubated in the dark with TUNEL solution for 1 h at 37 °C. A confocal laser scanning microscopy (Nikon A1) was utilized to capture HepG2/ADR cells images.

4.13 Animal models

All male BALB/c nude mice were obtained from Beijing Vital River Laboratory Animal Technology Co., Ltd. (Beijing, China). All animal experiments were conducted in compliance with the Institutional Animal Experiment Administration Committee of the Fourth Military Medical University. The mice were bred at the animal facilities of Xi'an Jiaotong University under the specific-pathogen-free conditions in the closed-top cages. The male BALB/c nude mice were eight weeks of age (18–22 g) and housed in an environmentally controlled room (temperature 22 ± 1 °C; relative humidity 55 ± 5 °C). They were given food and water *ad libitum*. BALB/c nude mice were subcutaneously injected into the groin with 2×10^6 HepG2/ADR cells to establish the tumor mouse model. When the tumor volume reached approxima100–150 mm^3, the mice were divided randomly into six groups (each group included 4 mice) and subjected to various treatments: (a) control group (0.2 mL of DPBS injection by intravenous), (b) Dox, (c) CeO_2, (d) CePA, (e) CeO_2 + Dox, and (f) CePA + Dox at 5 mg/kg Dox and 5 mg/kg. CeO_2/CePA via tail vein injection on the 1st and 8th day during the period of therapy (14 days), respectively. During the course of treatments, the mice body weights and tumor volumes in all groups were monitored every two days. Tumor volumes were calculated as follows: V = (width × width × length)/2. The relative tumor volumes were compared with that of the first day. After 14 days of treatment, all the mice were sacrificed with CO_2. The main organs (heart, liver, spleen, lung,

and kidney) and tumors of all mice were collected for histology analysis, TUNEL assay, and immunofluorescent staining.rescent staining.

4.14 Biodistribution of CeO_2 and CePA *in vivo*

Tumor-bearing BALB/c nude mice were injected with CeO_2 and CePA in a dosage of 5 mg/kg via tail vein injection. On the 1st day and the 7th day of the treatments, the mice humanely were sacrificed. The main organs (heart, liver, spleen, lung, and kidney) and tumor tissues were dissected, weighed, and homogenized. Subsequently, the main organs, tumor tissues, and urine samples were digested in aqua regia for 24 h. Afterwards, the solutions were diluted with water and filtered using 0.22 μm membrane. Finally, the Ce element content was determined by ICP-MS, which was repeatedly for three times.

4.15 Blood hemanalysis

Tumor-bearing BALB/c nude mice were intravenously injected with CeO_2 (5 mg/kg) and CePA (5 mg/kg), respectively. Blood samples were collected at 24 h post injection. The routine blood tests were carried out by an automatic hematology analyzer (BC-2800Vet, Mindray).

4.16 Blood biochemistry analysis

Tumor-bearing BALB/c nude mice were intravenously injected with CeO_2 (5 mg/kg) and CePA (5 mg/kg), respectively. After the treatments, the mice were sacrificed and the blood samples were collected for the cardiac and hepatic function analysis. The levels of alanine aminotransferase, aspartate aminotransferase, lactate dehydrogenase and creatine kinase isoenzyme myocardial band were determined by the Biochemical Auto Analyzer (Chemray800, Rayto).

4.17 HE, TUNEL, DHE, and immunofluorescent staining

The main organs and the separated solid tumors were washed with cold DPBS, then fixed with 4% formaldehyde at 4 °C for 24 h and then embedded in paraffin and sliced. The slices were stained with HE and the images were obtained by a light microscope. The apoptosis in heart, liver, and tumor tissue was also detected by TUNE staining (Beyotime). DHE staining was performed to test the ROS levels in heart, liver, and tumor tissues. In addition, the heart, liver and tumor tissues were stained with anti-caspase-3 antibody (Invitrogen, dilution 1:200) for immunohistochemistry analysis according to the following procedure. In order to prevent from nonspecific binding, the sections were blocked at 4 °C for 12 h in a blocking buffer containing 5% non-fat milk (Bio-Rad). Afterwards, the slices were incubated with the secondary antibody-FITC (1:50 dilution, Invitrogen) for 1 h at room temperature. After counterstained with DAPI, the slices were acquired with a confocal microscope (Nikon A1). Meantime, the apoptosis in tumor tissue was also detected by TUNE immunofluorescence staining (Beyotime Biotechnology).

4.18 Statistical snalysis

All data were expressed in this article as mean result ± standard deviation (SD). Statistical evaluation was performed using unpaired Student's two-sided *t* test analysis with Prism. Asterisks indicate significant differences ($^{**}P < 0.005$, $^{***}P < 0.001$, and $^{****}P < 0.0001$).

Acknowledgements

This work was financially supported by the National Natural Science Foundation of China (Nos. 52002314, 21872109, 81802841, and 81702999) and China Postdoctoral Science Foundation (Nos. 2018M633504 and 2018M633749). The study was also supported by the National Natural Science Foundation of Shaanxi Province (No. 2019JQ-486), the Natural Science Basic Research Plan in Shaanxi Province (No. 2019JM-033), and Technology Innovation Development Foundation of Tangdu Hospital (No. 2019QYTS003). Authors also acknowledge the support from the Fundamental Research Funds for the Central Universities (Nos. D5000210829 and G2021KY05102). We thank Miss Liu at Instrument Analysis Center of Xi'an Jiaotong University for her assistance with XPS tests. We are grateful to Xiaoli Qu (State Key Laboratory for Manufacturing Systems Engineering, Xi'an Jiaotong University) for assistance with confocal microscope assay. The authors are grateful to Yujing Xu (Centre for Plasma Biomedicine, State Key Laboratory of Electrical Insulation and Power Equipment, Xi'an Jiaotong University) for assistance with flow cytometry.

Electronic Supplementary Material: Supplementary material (further details of the XRD pattern of CeO_2, TEM images, XPS spectra, cellular uptake study, cytotoxicity data, apoptosis study, biodistribution, and biosecurity of nanocerias *in vivo*, etc.) is available in the online version of this article at https://doi.org/10.1007/s12274-022-4069-0.

References

[1] Hirabayashi, Y.; Kwon, S. K.; Paek, H.; Pernice, W. M.; Paul, M. A.; Lee, J.; Erfani, P.; Raczkowski, A.; Petrey, D. S.; Pon, L. A. et al. ER-mitochondria tethering by PDZD8 regulates Ca^{2+} dynamics in mammalian neurons. *Science* **2017**, *358*, 623–630.

[2] Clapham, D. E. Calcium signaling. *Cell* **2007**, *131*, 1047–1058.

[3] Trebak, M.; Kinet, J. P. Calcium signalling in T cells. *Nat. Rev. Immunol.* **2019**, *19*, 154–169.

[4] Monteith, G. R.; Prevarskaya, N.; Roberts-Thomson, S. J. The calcium-cancer signalling nexus. *Nat. Rev. Cancer* **2017**, *17*, 373–380.

[5] Guan, Q.; Zhou, L. L.; Lv, F. H.; Li, W. Y.; Li, Y. A.; Dong, Y. B. A glycosylated covalent organic framework equipped with BODIPY and $CaCO_3$ for synergistic tumor therapy. *Angew. Chem., Int. Ed.* **2020**, *59*, 18042–18047.

[6] Bao, Q. Q.; Hu, P.; Ren, W. W.; Guo, Y. D.; Shi, J. L. Tumor cell dissociation removes malignant bladder tumors. *Chem* **2020**, *6*, 2283–2299.

[7] Saurav, S.; Tanwar, J.; Ahuja, K.; Motiani, R. K. Dysregulation of host cell calcium signaling during viral infections: Emerging paradigm with high clinical relevance. *Mol. Aspects Med.* **2021**, *81*, 101004.

[8] Marchi, S.; Giorgi, C.; Galluzzi, L.; Pinton, P. Ca^{2+} fluxes and cancer. *Mol. Cell* **2020**, *78*, 1055–1069.

[9] Wang, Z. Q.; An, H. W.; Hou, D. Y.; Wang, M. D.; Zeng, X. Z.; Zheng, R.; Wang, L.; Wang, K. L.; Wang, H.; Xu, W. H. Addressable peptide self-assembly on the cancer cell membrane for sensitizing chemotherapy of renal cell carcinoma. *Adv. Mater.* **2019**, *31*, 1807175.

[10] Waghray, D.; Zhang, Q. H. Inhibit or evade multidrug resistance P-glycoprotein in cancer treatment. *J. Med. Chem.* **2018**, *61*, 5108–5121.

[11] Tuguntaev, R. G.; Chen, S. Z.; Eltahan, A. S.; Mozhi, A.; Jin, S. B.; Zhang, J. C.; Li, C.; Wang, P. C.; Liang, X. J. P-gp inhibition and mitochondrial impairment by dual-functional nanostructure based on Vitamin E derivatives to overcome multidrug resistance. *ACS Appl. Mater. Interfaces* **2017**, *9*, 16900–16912.

[12] Chen, X. K.; Zhang, X. D.; Guo, Y. X.; Zhu, Y. X.; Liu, X. Y.; Chen, Z.; Wu, F. G. Smart supramolecular " Trojan Horse" -inspired nanogels for realizing light-triggered nuclear drug influx in drug-resistant cancer cells. *Adv. Funct. Mater.* **2019**, *29*, 1807772.

[13] Chen, Z. W.; Wang, Z. J.; Gu, Z. Bioinspired and biomimetic nanomedicines. *Acc. Chem. Res.* **2019**, *52*, 1255–1264.

[14] Hu, Z. T.; Ding, Y. Cerium oxide nanoparticles-mediated cascade

catalytic chemo-photo tumor combination therapy. *Nano Res.* **2022**, *15*, 333–345.
[15] Jiang, S. X.; Ge, Z. L.; Mou, S.; Yan, H.; Fan, C. H. Designer DNA nanostructures for therapeutics. *Chem* **2021**, *7*, 1156–1179.
[16] Wu, H. Y.; Zhong, D.; Zhang, Z. J.; Li, Y. C.; Zhang, X.; Li, Y. K.; Zhang, Z. Z.; Xu, X. H.; Yang, J.; Gu, Z. W. Bioinspired artificial tobacco mosaic virus with combined oncolytic properties to completely destroy multidrug-resistant cancer. *Adv. Mater.* **2020**, *32*, 1904958.
[17] Chu, X.; Jiang, X. W.; Liu, Y. Y.; Zhai, S. J.; Jiang, Y. Q.; Chen, Y.; Wu, J.; Wang, Y.; Wu, Y. L.; Tao, X. F. et al. Nitric oxide modulating calcium store for Ca^{2+}-initiated cancer therapy. *Adv. Funct. Mater.* **2021**, *31*, 2008507.
[18] Wang, S.; Liu, X.; Chen, S. Z.; Liu, Z. R.; Zhang, X. D.; Liang, X. J.; Li, L. L. Regulation of Ca^{2+} signaling for drug-resistant breast cancer therapy with mesoporous silica nanocapsule encapsulated doxorubicin/siRNA cocktail. *ACS Nano* **2019**, *13*, 274–283.
[19] Gao, P.; Chen, Y. Y.; Pan, W.; Li, N.; Liu, Z.; Tang, B. Antitumor agents based on metal-organic frameworks. *Angew. Chem., Int. Ed.* **2021**, *60*, 16763–16776.
[20] Zhang, M.; Song, R. X.; Liu, Y. Y.; Yi, Z. G.; Meng, X. F.; Zhang, J. W.; Tang, Z. M.; Yao, Z. W.; Liu, Y.; Liu, X. G. et al. Calcium-overload-mediated tumor therapy by calcium peroxide nanoparticles. *Chem* **2019**, *5*, 2171–2182.
[21] Shen, S. Y.; Xu, X.; Lin, S. Q.; Zhang, Y.; Liu, H. Y.; Zhang, C.; Mo, R. A nanotherapeutic strategy to overcome chemotherapeutic resistance of cancer stem-like cells. *Nat. Nanotechnol.* **2021**, *16*, 104–113.
[22] Liu, J. J.; Zhu, C. Y.; Xu, L. H.; Wang, D. Y.; Liu, W.; Zhang, K. X.; Zhang, Z. Z.; Shi, J. L. Nanoenabled intracellular calcium bursting for safe and efficient reversal of drug resistance in tumor cells. *Nano Lett.* **2020**, *20*, 8102–8111.
[23] Zheng, P.; Ding, B. B.; Shi, R.; Jiang, Z. Y.; Xu, W. G.; Li, G.; Ding, J. X.; Chen, X. S. A multichannel Ca^{2+} nanomodulator for multilevel mitochondrial destruction-mediated cancer therapy. *Adv. Mater.* **2021**, *33*, 2007426.
[24] Li, Y. L.; Zhou, S.; Song, H. Z.; Yu, T.; Zheng, X. D.; Chu, Q. $CaCO_3$ nanoparticles incorporated with KAE to enable amplified calcium overload cancer therapy. *Biomaterials* **2021**, *277*, 121080.
[25] Bushinsky, D. A.; Monk, R. D. Electrolyte quintet: Calcium. *Lancet* **1998**, *352*, 306–311.
[26] Tang, N.; Li, H. H.; Zhang, L. H.; Zhang, X. Y.; Chen, Y. N.; Shou, H.; Feng, S. S.; Chen, X. H.; Luo, Y.; Tang, R. K. et al. A macromolecular drug for cancer therapy via extracellular calcification. *Angew. Chem., Int. Ed.* **2021**, *60*, 6509–6517.
[27] Ma, X.; Cai, Y. F.; He, D. X.; Zou, C.; Zhang, P.; Lo, C. Y.; Xu, Z. Y.; Chan, F. L.; Yu, S.; Chen, Y. et al. Transient receptor potential channel TRPC5 is essential for P-glycoprotein induction in drug-resistant cancer cells. *Proc. Natl. Acad. Sci. USA* **2012**, *109*, 16282–16287.
[28] Tsuruo, T.; Iida, H.; Kawabata, H.; Tsukagoshi, S.; Sakurai, Y. High calcium content of pleiotropic drug-resistant P388 and K562 leukemia and Chinese hamster ovary cells. *Cancer Res.* **1984**, *44*, 5095–5099.
[29] Nygren, P.; Larsson, R.; Gruber, A.; Peterson, C.; Bergh, J. Doxorubicin selected multidrug-resistant small cell lung cancer cell lines characterised by elevated cytoplasmic Ca^{2+} and resistance modulation by verapamil in absence of P-glycoprotein overexpression. *Br. J. Cancer* **1991**, *64*, 1011–1018.
[30] Moslehi, J. J. Cardiovascular toxic effects of targeted cancer therapies. *N. Engl. J. Med.* **2016**, *375*, 1457–1467.
[31] Coker, R. J.; James, N. D.; Stewart, J. S. W. Hepatic toxicity of liposomal encapsulated doxorubicin. *Lancet* **1993**, *341*, 756.
[32] Tian, Z. M.; Li, X. H.; Ma, Y. Y.; Chen, T.; Xu, D. H.; Wang, B. C.; Qu, Y. Q.; Gao, Y. Quantitatively intrinsic biomimetic catalytic activity of nanocerias as radical scavengers and their ability against H_2O_2 and doxorubicin-induced oxidative stress. *ACS Appl. Mater. Interfaces* **2017**, *9*, 23342–23352.
[33] Wang, C. P.; Li, L.; Zhang, S.; Yan, Y.; Huang, Q.; Cai, X. P.; Xiao, J. R.; Cheng, Y. Y. Carrier-free platinum nanomedicine for targeted cancer therapy. *Small* **2020**, *16*, 2004829.
[34] Kim, J. S.; Jang, S. W.; Son, M.; Kim, B. M.; Kang, M. J. Enteric-coated tablet of risedronate sodium in combination with phytic acid, a natural chelating agent, for improved oral bioavailability. *Eur. J. Pharm. Sci.* **2016**, *82*, 45–51.
[35] Cai, K.; Sun, F. X.; Liang, X. Q.; Liu, C.; Zhao, N.; Zou, X. Q.; Zhu, G. S. An acid-stable hexaphosphate ester based metal-organic framework and its polymer composite as proton exchange membrane. *J. Mater. Chem. A* **2017**, *5*, 12943–12950.
[36] Wu, J. J. X.; Wang, X. Y.; Wang, Q.; Lou, Z. P.; Li, S. R.; Zhu, Y. Y.; Qin, L.; Wei, H. Nanomaterials with enzyme-like characteristics (nanozymes): Next-generation artificial enzymes (II). *Chem. Soc. Rev.* **2019**, *48*, 1004–1076.
[37] Karakoti, A.; Singh, S.; Dowding, J. M.; Seal, S.; Self, W. T. Redox-active radical scavenging nanomaterials. *Chem. Soc. Rev.* **2010**, *39*, 4422–4432.
[38] Huang, Y. Y.; Ren, J. S.; Qu, X. G. Nanozymes: Classification, catalytic mechanisms, activity regulation, and applications. *Chem. Rev.* **2019**, *119*, 4357–4412.
[39] Li, Y. Y.; He, X.; Yin, J. J.; Ma, Y. H.; Zhang, P.; Li, J. Y.; Ding, Y. Y.; Zhang, J.; Zhao, Y. L.; Chai, Z. F. et al. Acquired superoxide-scavenging ability of ceria nanoparticles. *Angew. Chem., Int. Ed.* **2015**, *54*, 1832–1835.
[40] Soh, M.; Kang, D. W.; Jeong, H. G.; Kim, D.; Kim, D. Y.; Yang, W.; Song, C.; Baik, S.; Choi, I. Y.; Ki, S. K. et al. Ceria-zirconia nanoparticles as an enhanced multi-antioxidant for sepsis treatment. *Angew. Chem., Int. Ed.* **2017**, *56*, 11399–11403.
[41] Liu, B. W.; Liu, J. W. Surface modification of nanozymes. *Nano Res.* **2017**, *10*, 1125–1148.
[42] Weng, Q. J.; Sun, H.; Fang, C. Y.; Xia, F.; Liao, H. W.; Lee, J.; Wang, J. C.; Xie, A.; Ren, J. F.; Guo, X. et al. Catalytic activity tunable ceria nanoparticles prevent chemotherapy-induced acute kidney injury without interference with chemotherapeutics. *Nat. Commun.* **2021**, *12*, 1436.
[43] Ren, Q. J.; Sun, S.; Zhang, X. D. Redox-active nanoparticles for inflammatory bowel disease. *Nano Res.* **2021**, *14*, 2535–2557.
[44] Li, J.; Zhang, Z. Y.; Tian, Z. M.; Zhou, X. M.; Zheng, Z. P.; Ma, Y. Y.; Qu, Y. Q. Low pressure induced porous nanorods of ceria with high reducibility and large oxygen storage capacity: Synthesis and catalytic applications. *J. Mater. Chem. A* **2014**, *2*, 16459–16466.
[45] Barron, L.; Nesterenko, P. N.; Diamond, D.; O'Toole, M.; Lau, K. T.; Paull, B. Low pressure ion chromatography with a low cost paired emitter-detector diode based detector for the determination of alkaline earth metals in water samples. *Anal. Chim. Acta* **2006**, *577*, 32–37.
[46] Fan, K. L.; Xi, J. Q.; Fan, L.; Wang, P. X.; Zhu, C. H.; Tang, Y.; Xu, X. D.; Liang, M. M.; Jiang, B.; Yan, X. Y. et al. *In vivo* guiding nitrogen-doped carbon nanozyme for tumor catalytic therapy. *Nat. Commun.* **2018**, *9*, 1440.
[47] Sang, Y. J.; Cao, F. F.; Li, W.; Zhang, L.; You, Y. W.; Deng, Q. Q.; Dong, K.; Ren, J. S.; Qu, X. G. Bioinspired construction of a nanozyme-based H_2O_2 homeostasis disruptor for intensive chemodynamic therapy. *J. Am. Chem. Soc.* **2020**, *142*, 5177–5183.
[48] Tian, Z. M.; Yang, K. L.; Yao, T. Z.; Li, X. H.; Ma, Y. Y.; Qu, C. Y.; Qu, X. L.; Xu, Y. J.; Guo, Y. H.; Qu, Y. Q. Catalytically selective chemotherapy from tumor-metabolic generated lactic acid. *Small* **2019**, *15*, 1903746.
[49] Zhu, H. M.; Cao, G. D.; Fu, Y. K.; Fang, C.; Chu, Q.; Li, X.; Wu, Y. L.; Han, G. R. ATP-responsive hollow nanocapsules for DOX/GOx delivery to enable tumor inhibition with suppressed P-glycoprotein. *Nano Res.* **2021**, *14*, 222–231.
[50] Tai, W. Y.; Gao, X. H. Ribonucleoprotein: A biomimetic platform for targeted siRNA delivery. *Adv. Funct. Mater.* **2019**, *29*, 1902221.
[51] Liu, X.; Qiu, Y.; Liu, Y. H.; Huang, N.; Hua, C.; Wang, Q. Q.; Wu, Z. Q.; Lu, J. X.; Song, P.; Xu, J. et al. Citronellal ameliorates doxorubicin-induced hepatotoxicity via antioxidative stress, antiapoptosis, and proangiogenesis in rats. *J. Biochem. Mol. Toxicol.* **2021**, *35*, e22639.